

Crystalline InGaZnO quaternary nanowires with superlattice structure for high-performance thin-film transistors

Fangzhou Li¹, SenPo Yip^{1,2,3}, Ruoting Dong^{1,2}, Ziyao Zhou^{1,2}, Changyong Lan¹, Xiaoguang Liang¹, Dapan Li¹, You Meng¹, Xiaolin Kang¹, and Johnny C. Ho^{1,2,3,4} (✉)

¹ Department of Materials Science and Engineering, City University of Hong Kong, Hong Kong 999077, China

² Shenzhen Research Institute, City University of Hong Kong, Shenzhen 518057, China

³ State Key Laboratory of Terahertz and Millimeter Waves, City University of Hong Kong, Hong Kong 999077, China

⁴ Centre for Functional Photonics, City University of Hong Kong, Hong Kong 999077, China

© Tsinghua University Press and Springer-Verlag GmbH Germany, part of Springer Nature 2019

Received: 21 March 2019 / Revised: 30 April 2019 / Accepted: 10 May 2019

ABSTRACT

Amorphous indium–gallium–zinc oxide (a-IGZO) materials have been widely explored for various thin-film transistor (TFT) applications; however, their device performance is still restricted by the intrinsic material issues especially due to their non-crystalline nature. In this study, highly crystalline superlattice-structured IGZO nanowires (NWs) with different Ga concentration are successfully fabricated by enhanced ambient-pressure chemical vapor deposition (CVD). The unique superlattice structure together with the optimal Ga concentration (i.e., 31 at.%) are found to effectively modulate the carrier concentration as well as efficiently suppress the oxygen vacancy formation for the superior NW device performance. In specific, the $\text{In}_{1.8}\text{Ga}_{1.8}\text{Zn}_{2.4}\text{O}_7$ NW field-effect transistor exhibit impressive device characteristics with the average electron mobility of $\sim 110 \text{ cm}^2\cdot\text{V}^{-1}\cdot\text{s}^{-1}$ and on/off current ratio of $\sim 10^6$. Importantly, these NWs can also be integrated into NW parallel arrays for the construction of high-performance TFT devices, in which their performance is comparable to many state-of-the-art IGZO TFTs. All these results can evidently indicate the promising potential of these crystalline superlattice-structured IGZO NWs for the practical utilization in next-generation metal-oxide TFT device technologies.

KEYWORDS

InGaZnO, nanowires, thin-film transistors, superlattice

1 Introduction

In the past decade, due to the high carrier mobility, excellent chemical and electrical stability, unique optical properties as well as relatively low processing temperatures [1–4], amorphous or polycrystalline metal-oxide thin-film semiconductors, such as indium gallium zinc oxide (IGZO), have attracted a lot of attention for many technological applications in high-performance thin-film transistors (TFTs), photodetectors, thermoelectric devices and others [5–11]. Despite many recent advances, there are still inevitably several drawbacks associated with these amorphous or polycrystalline thin-film based electrical devices for practical utilizations. One issue is that their carrier mobility would get substantially degraded by the scattering at grain boundaries, while another problem comes from the existence of large amounts of oxygen vacancy making them difficult to control their carrier concentration for the efficient device off-state current suppression [12, 13]. It is witnessed that crystalline IGZO materials can minimize their carrier scattering and oxygen vacancy content to significantly improve their device performance [14]. For example, high-quality, crystalline and layered superlattice structure of IGZO TFT device channels have been uniquely developed with superior electrical properties, in which the alternatively stacked configuration of InO^{2+} layers and $\text{GaO}(\text{ZnO})^{5+}$ blocks can contribute the efficient modulation of carrier concentration together with the suppression of oxygen vacancy formation and minimization of grain-boundary potential barriers [15]. In particular,

$\text{RMO}_3(\text{ZnO})_m$ (R = rare earth elements; M = In, Ga, Fe, or Al) is one type of materials with a large flexibility to modulate the chemical composition and the superlattice period. Such a multi-layered structure has been regarded as a so-called “natural superlattice”, acting as a multi-quantum-well, which exhibits exceptional properties originating from the spatial confinement of electrons in the two-dimensional layer [15, 16]. In any case, it is quite a complex process to fabricate these crystalline IGZO films since single-crystal yttria-stabilized zirconia (YSZ) substrates, multiple pulsed laser deposition (PLD) steps and thermal annealing procedures with the temperature up to 1,400 °C for 30 min in ambient are needed [15–18]; therefore, these thin-film channels would not be easily compatible with many device platforms.

Fortunately, because of the advent of nanotechnology, it becomes feasible to achieve crystalline IGZO materials in the nanoscale configuration, particularly one-dimensional nanowires (NWs), with conventional synthesis techniques and mild process conditions [19–21]. In specific, Felizzo et al. presented the successful growth of highly-crystalline IGZO NWs from amorphous IGZO thin films using the bimetal-catalyzed vapor-liquid-solid (VLS) mechanism with a relatively low temperature (700 °C), but the NWs were only found to grow on the catalyst edge with a low density [22]. Similarly, Li and his team established a synthesis technique to obtain crystalline IGZO NWs with superlattice structures via the Au-assisted VLS scheme at 1,400 °C; however, the NW surface was very rough with a significant tapering phenomenon [23]. To the best of our knowledge,

besides the thorough structural characterization, no electrical device characteristics of the crystalline IGZO NWs have been reported [22, 23]. As a result, it is necessary to develop the mild synthesis techniques and to thoroughly study the electrical properties of IGZO NWs, especially the effect of NW stoichiometry on their electrical device characteristics for practical utilizations.

In this work, high-quality and crystalline IGZO NWs with controllable stoichiometry have been successfully prepared by the enhanced ambient-pressure chemical vapor deposition (CVD) method. Importantly, the obtained NWs exhibit the perfect superlattice structure with alternately stacking of InO^{2-} layers and $\text{InGaO}(\text{ZnO})^{4+}$ blocks forming a periodic layered structure. Similar to the previously reported superlattice IGZO thin films, this superlattice structure configured in the NW geometry together with the Ga incorporation can effectively suppress the oxygen vacancy formation, contributing to the superior electrical device properties when the IGZO NW field-effect transistors (FETs) are fabricated. It is noted that the electron mobility of NWFETs can as well be manipulated by tuning the Ga concentration of IGZO NWs. When the Ga concentration increases, the device electron mobility improves accordingly with a maximum value of $110 \text{ cm}^2 \cdot \text{V}^{-1} \cdot \text{s}^{-1}$ at the optimal atomic Ga concentration of 31% (i.e., $\text{In}_{1.8}\text{Ga}_{1.8}\text{Zn}_{2.4}\text{O}_7$) alongside the impressive device on/off current ratio of around 10^6 . For the further increasing Ga concentration, the mobility would be degraded correspondingly, which can be attributed to the deteriorated lattice structure caused by the excessive amount of Ga. Regardless, highly-ordered IGZO NW parallel arrays can also be constructed with the respectable TFT device performance. All these results can evidently indicate the potential of these crystalline superlattice-structured IGZO NWs for the hands-on realization of next-generation metal-oxide TFT device technologies.

2 Experimental section

2.1 Synthesis of IGZO and IZO NWs

Here, IGZO NWs and control samples of indium–zinc oxide (IZO) NWs were grown on the surface of Si/SiO₂ (50-nm-thick thermal oxide) substrates by the ambient-pressure CVD method. The substrates were first deposited with a thin layer of Au film (0.1 nm in the nominal thickness) by thermal evaporation, where these films were used as the catalysts. For the growth of IGZO NWs, a varied mass of Ga granules (0.023–0.115 g in mass; 1–2 mm in size; 99.999% in purity; China Rare Metal), a fixed mass of 0.38 g of In granules (1–2 mm in size; 99.999% in purity; China Rare Metal) and 0.0022 g of zinc powder (20–30 mesh; > 99.8% in purity; Sigma-Aldrich) mixed with 0.3 g of graphite powder (< 20 μm in size, synthetic; Sigma-Aldrich) were used as the precursor source. During the growth, the source was placed at the sealed end of a quartz tube (10 cm in length and 1 cm in diameter) while the substrate, predeposited with the catalyst, was positioned 2 cm away from the source. This quartz tube was then put in the center of a large quartz tube (1 inch in diameter) within the single-zone horizontal tube furnace. Next, the set-up was heated up to 990 °C in 20 min and held for 7 min with the flow rate of gas mixture (10 vol.% (oxygen) + 90 vol.% (argon)) and argon (99.9995% in purity) maintained at 20 and 80 sccm, respectively. When the growth was done, the system was naturally cooled to the room temperature. This growth process was then repeated twice (i.e., 2nd and 3rd growth runs) with fresh substrates but using the same precursor source. It is noted that the 3rd growth was held at 990 °C for 10 min. As shown in Fig. S1 in the Electronic Supplementary Material (ESM), pure ZnO and In doped ZnO (e.g., $\text{In}_{0.016}\text{Zn}_{0.984}\text{O}$) NWs were collected for the first two growth runs, respectively, while IGZO NWs with different chemical stoichiometry could be reliably obtained after the 3rd growth run. In this case, we employed this growth sequence to controllably fabricate

the IGZO NWs based on the continuous depletion of different constituents in the precursor source. Specifically, simply by varying the mass of the starting Ga source, four different NW sample groups (IGZO NWs with different composition) could be achieved, namely $\text{In}_{0.3}\text{Ga}_{3.9}\text{Zn}_{1.8}\text{O}_7$, $\text{In}_{1.8}\text{Ga}_{1.8}\text{Zn}_{2.4}\text{O}_7$, $\text{In}_{2.4}\text{Ga}_{0.3}\text{Zn}_{3.3}\text{O}_7$, and $\text{Zn}_4\text{In}_2\text{O}_7$ (control sample grown without using any Ga source) NWs. These NW composition are actually determined by the subsequent chemical characterization. Importantly, all these NW samples have been repeated for at least 5 times with the metal constituents varying less than 3 at.%, indicating the reliable control of their composition using this growth sequence (Fig. S2 in the ESM).

2.2 Material characterization

X-ray diffraction (XRD, D2 Phaser, Bruker) was used to analyze the crystal structure of the obtained NWs. The morphologies of as-prepared products were examined using a scanning electron microscope (SEM, Quanta 450 FEG, FEI) and a transmission electron microscope (TEM, CM 20). High-resolution TEM (HRTEM, JEOL-2001F) and selected area electron diffraction (SAED) were also performed to assess the crystallinity of the NWs. Energy dispersive X-ray spectrometry (EDS) and corresponding elemental mappings were employed to evaluate the chemical composition of the NWs.

2.3 Fabrication and electrical measurement of IGZO and IZO NW transistors

At first, the NWs were dispersed in 2-propanol solution by ultrasonication. Next, the solution mixture was drop-casted on the surface of boron-doped Si substrates with a 50-nm-thick thermally grown oxide layer, followed by standard photolithography to define the source and drain electrode regions. Then, electron beam evaporation was used to deposit the 80-nm thick Ni film. The lift-off process was subsequently performed to obtain the electrodes. At the end, electrical performance of the fabricated NW FET devices were evaluated by using a standard probe station with an Agilent 4155C semiconductor analyzer (Agilent Technologies, Santa Clara, CA, USA). All electrical measurement were performed in the clockwise direction.

3 Results and discussion

In this work, IGZO NWs are successfully fabricated by ambient-pressure CVD with different starting mass of Ga precursor. As shown in the scanning electron microscopy (SEM) images in Fig. 1, all samples exhibit the well-defined NW morphology with the smooth surface and the length of tens of micrometers. Their crystal structures are then assessed by X-ray diffraction (XRD). It is clear that all the diffraction peaks of Ga alloyed NW samples can be indexed to the hexagonal structure of $\text{InGaZn}_4\text{O}_7$ (PDF No. 40-0254) while the ones of pure indium-zinc oxide (IZO) NWs (control sample) can be corresponded to the hexagonal structure of $\text{Zn}_4\text{In}_2\text{O}_7$ (PDF No. 20-1438) (Fig. S3 in the ESM). Apart from the peak of ZnO (110) and substrate peak of Si (200), there are not any other impurity phases observed, which indicate the phase purity of our grown NWs. After that, the NW composition is evaluated by energy dispersive X-ray spectrometry (EDS). Although EDS may not be an accurate technique to evaluate the oxygen concentration of the obtained samples, it can still provide precise and reliable composition information of the metallic components of the grown NWs (Fig. S4 in the ESM). The Ga concentration is defined as $\text{Ga}(\text{at.}\%)/(\text{In}(\text{at.}\%) + \text{Ga}(\text{at.}\%) + \text{Zn}(\text{at.}\%))$ such that the constituent composition expressed in at.% is accurately assessed by EDS. Combined with the XRD results, the samples can be determined to be $\text{Zn}_4\text{In}_2\text{O}_7$, $\text{In}_{2.4}\text{Ga}_{0.3}\text{Zn}_{3.3}\text{O}_7$, $\text{In}_{1.8}\text{Ga}_{1.8}\text{Zn}_{2.4}\text{O}_7$ and $\text{In}_{0.3}\text{Ga}_{3.9}\text{Zn}_{1.8}\text{O}_7$ NWs with the increasing Ga concentration of 0 at.%, 5 at.%, 31 at.%, and 66 at.%, as presented in Figs. 1(a)–1(d), respectively. More importantly, spherical-like catalytic seeds are seen at the NW tips,

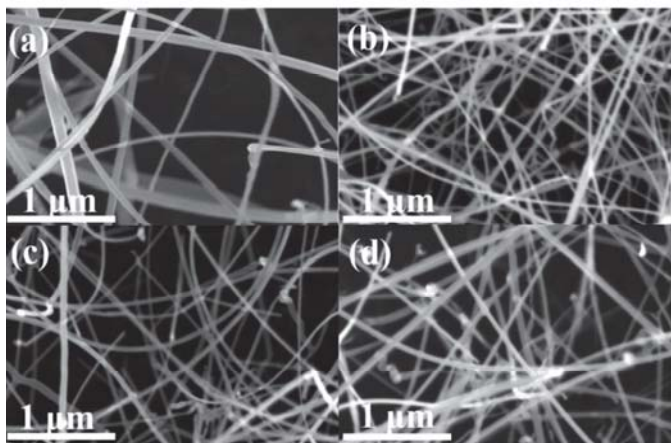


Figure 1 SEM studies of NW samples grown with the increasing mass of Ga precursor. SEM images of (a) $\text{Zn}_4\text{In}_2\text{O}_7$, (b) $\text{In}_{2.4}\text{Ga}_{0.3}\text{Zn}_{3.3}\text{O}_7$, (c) $\text{In}_{1.8}\text{Ga}_{1.8}\text{Zn}_{2.4}\text{O}_7$ and (d) $\text{In}_{0.3}\text{Ga}_{3.9}\text{Zn}_{1.8}\text{O}_7$. The NW compositions are determined by compiling the results of XRD and EDS.

suggesting the IGZO NW growth follows the commonly observed vapor-liquid-solid (VLS) mechanism [24–27]. However, even though the same catalytic film thickness is used for all the NW synthesis here, it is interesting that the NW diameter distribution extracted from the transmission electron microscopy (TEM) images is quite different among the samples (Fig. S5 in the ESM). Evidently, the NW diameter gets substantially reduced when Ga is alloyed into the material system. For example, the diameter of $\text{Zn}_4\text{In}_2\text{O}_7$ NWs is determined to be 60 ± 20 nm based on the statistics of more than 50 individual NWs in each sample group. Once Ga is introduced into the NW lattice, the diameter is shrunk to 32 ± 15 nm, 26 ± 12 nm and 34 ± 11 nm for $\text{In}_{2.4}\text{Ga}_{0.3}\text{Zn}_{3.3}\text{O}_7$, $\text{In}_{1.8}\text{Ga}_{1.8}\text{Zn}_{2.4}\text{O}_7$, and $\text{In}_{0.3}\text{Ga}_{3.9}\text{Zn}_{1.8}\text{O}_7$ NWs, accordingly. This diameter reduction is perfectly consistent with the previous studies that the Ga alloying can decrease the radial NW growth to achieve the thin and uniform NWs [28, 29]. It is due to the fact that the presence of Ga during the growth process can decrease the source metal vapor pressure as Ga has a vapor pressure a lot smaller than the one of In at the same conditions. This decreased metal vapor pressure would then lead to a reduced suppression of the limited oxygen content in the carrier gas, which facilitates the transport of oxygen vapor for the NW

growth, yielding to the higher longitudinal and the lower radial growth rates of NWs [28, 29].

In addition, detailed TEM studies are as well carried out to evaluate the morphology and crystallinity of the grown NWs. As depicted in Figs. 2(a)–2(d), the surface of fabricated NWs is very smooth and the diameter of IZO NWs is around 70 nm, being much larger than that of IGZO NWs. The dominant growth orientation of each NW sample group is also determined, in which all these findings are in the good agreement with SEM and XRD results discussed above. Interestingly, when SAED patterns are collected for the NW samples, there are diffraction spots consisting of a mixture of primary and satellite dots. To be specific, there are five satellite spots located between every two adjacent main spots, where these satellite diffraction spots are the characteristic feature of the superlattice structure [30]. Almost all the NWs we observed have the same diffraction feature. Indeed, when HRTEM is performed as illustrated in Figs. 2(e)–2(h), the periodic dark-bright layered structures are obviously witnessed in all the samples, elucidating the formation of the superlattice structure [31–33]. Similar to the previous report on $\text{InAlO}_3(\text{ZnO})_{15}$ superlattice-structured NWs [13], for the case of $\text{Zn}_4\text{In}_2\text{O}_7$ NWs, InO^{2-} and $\text{InO}(\text{ZnO})^{4+}$ layers can be identified and denoted as the In-O layer and In/Zn-O block, respectively. Figure 2(e) demonstrates clearly that there are five In/Zn-O layers (thin dark lines) existed between every two adjacent In-O layers (thick dark lines), which further confirms the presence of In-O octahedral layers periodically interleaved by In/Zn-O layers (Fig. 2(e)) [34, 35]. This finding is also consistent with the crystal structure of $\text{Zn}_4\text{In}_2\text{O}_7$ observed in XRD (Fig. S3 in the ESM). In this case, the lattice constant, c , equivalent to two times of the distance between two adjacent In-O layers [36], is determined to be 3.4 nm for the $\text{Zn}_4\text{In}_2\text{O}_7$ NW. Once the Ga species are introduced, they are observed to replace In in the In/Zn-O layers to yield the mixed In,Ga/Zn-O layers whereas the In-O octahedral layers are maintained (Figs. 2(f)–2(h)). This In substitution by Ga (the smaller ion radius) is also reflected by the continuous reduction of the c parameter for NWs with the increasing Ga concentration [37]. For example, the c parameter is found to reduce from 3.4 nm for $\text{Zn}_4\text{In}_2\text{O}_7$ NWs, to 3.31 nm for $\text{In}_{2.4}\text{Ga}_{0.3}\text{Zn}_{3.3}\text{O}_7$ NWs, 3.18 nm for $\text{In}_{1.8}\text{Ga}_{1.8}\text{Zn}_{2.4}\text{O}_7$ NWs, and 2.94 nm for $\text{In}_{0.3}\text{Ga}_{3.9}\text{Zn}_{1.8}\text{O}_7$ NWs. Actually, Ga has been demonstrated to play a very important role in the synthesis of perfect superlattice structures as well as to modulate the distance

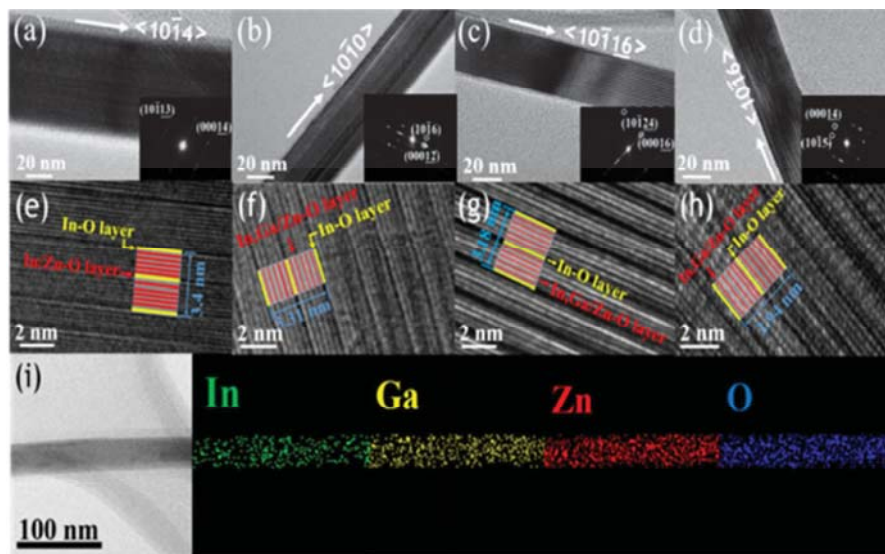


Figure 2 TEM studies of NW samples grown with the increasing mass of Ga precursor. (a)–(d) TEM images and the corresponding SAED patterns of $\text{Zn}_4\text{In}_2\text{O}_7$, $\text{In}_{2.4}\text{Ga}_{0.3}\text{Zn}_{3.3}\text{O}_7$, $\text{In}_{1.8}\text{Ga}_{1.8}\text{Zn}_{2.4}\text{O}_7$ and $\text{In}_{0.3}\text{Ga}_{3.9}\text{Zn}_{1.8}\text{O}_7$ NWs, respectively. (e)–(h) HRTEM images of the NWs presented in the panel (a) to (d), accordingly. (i) Scanning TEM image of the $\text{In}_{1.8}\text{Ga}_{1.8}\text{Zn}_{2.4}\text{O}_7$ NW along with the elemental mappings of In, Ga, Zn and O, respectively.

between In-O layers [23]. In this case, these superlattice structures can be made perfect in a qualitative sense (i.e., steaky SAED pattern in Fig. 3(g)) by increasing the Ga concentration to an optimal level (e.g., 31 at.%) to give the stoichiometric structure of $\text{InGaO}_3(\text{ZnO})_4$, being consistent with the crystal structure of $\text{InGaZn}_4\text{O}_7$ determined in XRD, but further raising the Ga concentration would partly destroy the superlattice structure as one can notice the unclearness in the SAED pattern in Fig. 2(d) and HRTEM image in Fig. 2(h). At the same time, scanning TEM (STEM) together with chemical mappings of the constituent species are executed on individual NWs (Fig. S6 in the ESM). The elements of In, Ga, Zn, and O are seen to distribute uniformly within the entire $\text{In}_{1.8}\text{Ga}_{1.8}\text{Zn}_{2.4}\text{O}_7$ NW (Fig. 2(i)). All these results can clearly indicate the smooth surface, excellent crystallinity and reliable composition control of the obtained superlattice-structured IGZO NWs.

In order to explore the electrical properties of IGZO NWs, FET devices based on individual NWs are fabricated. Specifically, as depicted in Fig. 3(a), a typical $\text{In}_{1.8}\text{Ga}_{1.8}\text{Zn}_{2.4}\text{O}_7$ NW is configured as the device channel on a degenerately boron doped Si substrate. The overgrown 50 nm thick thermal oxide is used as the gate dielectric, while 80 nm thick Ni films are employed as the source/drain electrodes to achieve a simple NW FET constructed in a global back-gated geometry. The corresponding transfer and output characteristics of the NW device are first measured in ambient conditions (Figs. S7(a) and S7(b) in the ESM). It is observed that there is a significant hysteresis associated with the transfer characteristics, which can be attributed to the adsorption of surrounding gases onto the unpassivated device channel. Subsequently, with the aim to assess the fundamental properties of NWs, all the electrical measurement are carried out in vacuum (5×10^{-4} Pa) to minimize the interaction between device channels and surrounding ambients as well as the device hysteresis effect. Based on the transfer characteristics presented in Fig. 3(b), the NW device demonstrates a clear n-type semiconducting behavior [38]. Under a source bias (V_{DS}) of 1 V, it can achieve an on-state current of 1.3 μA at a gate bias (V_{GS}) of 40 V and an off-state current of 1.9 pA at a V_{GS} of -5 V. This on/off current ratio can be as high as 7×10^5 , which is important for practical device applications. Besides, the linear relationship displayed in the output characteristics in Fig. 3(c) can confirm the ohmic-like contact behavior between the NW channel and the electrodes. Importantly,

the field-effect electron mobility (μ_{FE}) of the device can be calculated as a function of V_{GS} as shown in Fig. 3(d). In details, the μ_{FE} value is extracted by the standard square law model of $\mu_{\text{FE}} = g_{\text{m}}(L^2/C_{\text{ox}})(1/V_{\text{DS}})$, where g_{m} is the transconductance and it is determined following the relationship of $g_{\text{m}} = (dI_{\text{DS}})/(dV_{\text{GS}})$ at a constant V_{DS} . L is the channel length and C_{ox} is the gate capacitance, which is calculated from the finite element analysis software COMSOL [39, 40]. At first, the gate capacitance per a unit length (C_{ox}) can be determined for a specific nanowire diameter (Fig. S8 in the ESM). Then, the C_{ox} is calculated by the equation of $C_{\text{ox}} = c_{\text{ox}}L$, where L is the length of the nanowire. This way, the peak mobility of $\text{In}_{1.8}\text{Ga}_{1.8}\text{Zn}_{2.4}\text{O}_7$ NW FET is found to be $\sim 110 \text{ cm}^2 \cdot \text{V}^{-1} \cdot \text{s}^{-1}$ (Fig. 3(d)). Statistical results of the peak field-effect electron mobility of more than 40 NW FETs are also compiled with the average mobility value of $108 \pm 30 \text{ cm}^2 \cdot \text{V}^{-1} \cdot \text{s}^{-1}$. This relatively narrow mobility variation can be attributed to the difference of NW surface roughness, crystallinity, and many other factors that can influence the electrical properties of the NW FETs.

Simultaneously, it is critical to explore the effect of different Ga concentration on the electrical properties of IGZO NW devices. In specific, the output characteristics of all devices also give the linear relationship between I_{DS} and V_{DS} , confirming the ohmic-like contact properties of the devices (Fig. S9 in the ESM). Utilizing the same device geometry, the FET device based on the individual IZO NW can deliver a high on-state current of 4.3 μA ($V_{\text{DS}} = 1$ V) but a very poor on/off current ratio of only ~ 30 as compared with those of other IGZO NW devices. By first introducing Ga into the NWs, the on-state current is found to drop to 1.1 μA ($V_{\text{DS}} = 1$ V), which can be related to the smaller NW diameter of $\text{In}_{2.4}\text{Ga}_{0.3}\text{Zn}_{3.3}\text{O}_7$ for the reduced effective channel width (Fig. S5 in the ESM). When the Ga concentration further increases, although the NW diameter stays relatively the same, the device on-state current would first slightly increased to 1.3 μA for the $\text{In}_{1.8}\text{Ga}_{1.8}\text{Zn}_{2.4}\text{O}_7$ NW and then substantially decreased to only 0.15 μA for the $\text{In}_{0.3}\text{Ga}_{3.9}\text{Zn}_{1.8}\text{O}_7$ NW. The on/off current ratio and mobility of all these samples follow the similar but the opposite trend. The on/off current ratio and mobility values would first increase from ~ 30 and $43 \text{ cm}^2 \cdot \text{V}^{-1} \cdot \text{s}^{-1}$ ($\text{Zn}_4\text{In}_2\text{O}_7$ NW) to 3×10^5 and $78 \text{ cm}^2 \cdot \text{V}^{-1} \cdot \text{s}^{-1}$ ($\text{In}_{2.4}\text{Ga}_{0.3}\text{Zn}_{3.3}\text{O}_7$ NW), then to 7×10^5 and $110 \text{ cm}^2 \cdot \text{V}^{-1} \cdot \text{s}^{-1}$ ($\text{In}_{1.8}\text{Ga}_{1.8}\text{Zn}_{2.4}\text{O}_7$ NW), and subsequently decrease to 2×10^5 and $40 \text{ cm}^2 \cdot \text{V}^{-1} \cdot \text{s}^{-1}$ ($\text{In}_{0.3}\text{Ga}_{3.9}\text{Zn}_{1.8}\text{O}_7$ NW), respectively. Moreover, the device threshold voltage (V_{th}) can be directly estimated

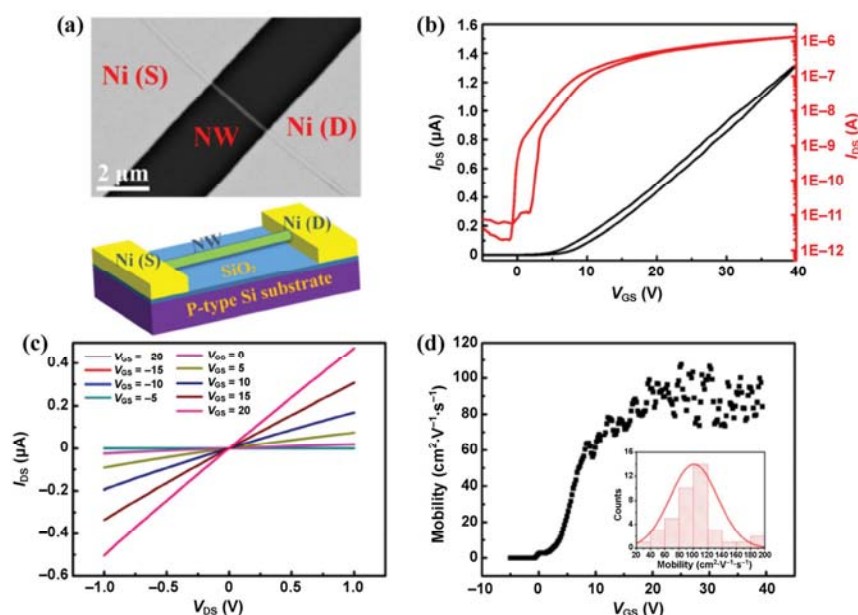


Figure 3 Electrical characterization of a typical FET based on a single $\text{In}_{1.8}\text{Ga}_{1.8}\text{Zn}_{2.4}\text{O}_7$ NW under vacuum. (a) SEM image and the schematic illustration of the FET device. (b) Transfer characteristics of the device ($V_{\text{DS}} = 1$ V). (c) Output characteristics of the device. (d) Field-effect electron mobility assessment for the same device presented in (b) and (c) with $V_{\text{DS}} = 1$ V. The inset shows the statistics of field-effect mobility based on 40 devices.

from the transfer characteristics (Fig. S10 in the ESM) and the corresponding free carrier concentration (n) can as well be determined following the analytical equation of $n = |(4C_{\text{ox}}V_{\text{th}})/(\pi qd^2L)|$, where q is the charge of an electron and d is the diameter of the NW [41, 42]. It seems that increasing the Ga concentration can suppress the formation of free carrier concentration of the NW devices. All these data trends are as well statistically depicted in Fig. 4 and Fig. S11 in the ESM. Obviously, the device performance is maximized with the mobility of $110 \text{ cm}^2\text{V}^{-1}\text{s}^{-1}$ and on/off current ratio of 7×10^5 for the $\text{In}_{1.8}\text{Ga}_{1.8}\text{Zn}_{2.4}\text{O}_7$ NW exhibiting the perfect superlattice structure among all samples. Further increasing the Ga concentration would start to degrade the NW device performance, which is probably due to the deteriorated superlattice structure.

To shed light on the enhancement of the device performance of $\text{In}_{1.8}\text{Ga}_{1.8}\text{Zn}_{2.4}\text{O}_7$ superlattice-structured NW transistors, thorough XPS investigation is performed. Figure S12(a) in the ESM shows the survey spectra of all the NW samples. There are not any other elemental peaks except for the ones of Zn, In, Ga, O, and C (from the atmospheric contamination due to air exposure) observed, further confirming the quaternary composition of the NWs. Furthermore, Figs. S12(b) and S12(c) in the ESM demonstrate the corresponding

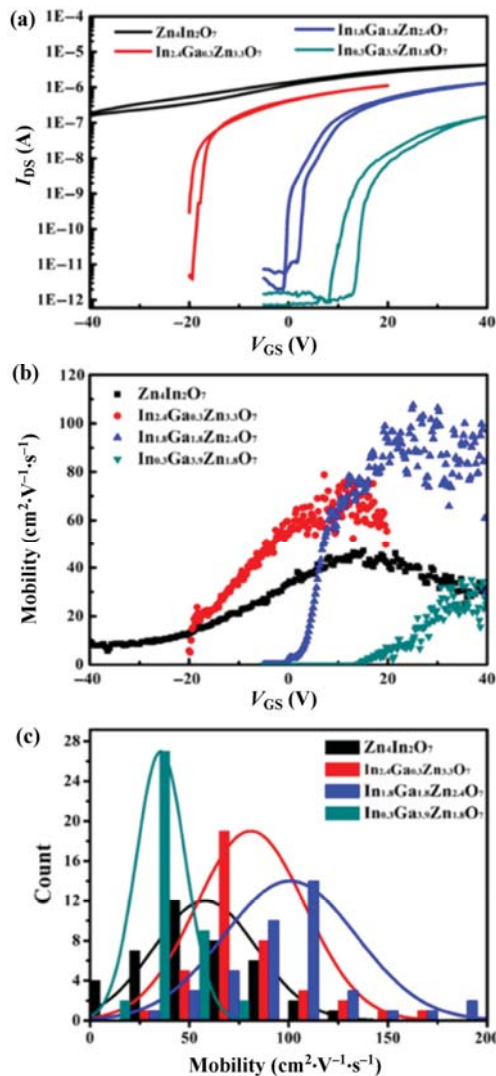


Figure 4 Electrical characterization of typical FET based on different individual IGZO and IZO NWs under vacuum. (a) Transfer characteristics of the devices ($V_{\text{DS}} = 1 \text{ V}$). (b) Field-effect electron mobility assessment for the devices presented in (a) with $V_{\text{DS}} = 1 \text{ V}$. (c) Statistics of the peak field-effect electron mobility of the devices. In each sample group, 40 different NW devices are evaluated with the Gaussian fitting performed.

high-resolution spectra of Zn 2p_{3/2} and In 3d, respectively. There are slight shifts of the Zn 2p_{3/2} and In 3d peaks for IGZO NWs as compared with those of IZO NWs that can be mainly due to the size effect as reported in the literature [43, 44]. Besides, for IGZO NWs, by increasing the Ga concentration, the bond energy associated with both Zn 2p_{3/2} and In 3d peaks exhibit the positive shift, which can be attributed to the electron transfer from Zn and In to Ga as Ga and O have the stronger electronic interaction than those of Zn and In with O [45]. More importantly, when the high-resolution O 1s spectra are collected for all the samples, the spectra can be deconvoluted into three types of oxygen levels (Fig. 5) [46]. Typically, the O_I peak at the lower binding energy ($\sim 529.5 \text{ eV}$) is ascribed to the substituted O^{2-} ions in the crystal lattice. The O_{II} peak with the medium binding energy ($\sim 530.8 \text{ eV}$) is corresponded to the oxygen related defects (e.g., vacancies) within the structure, while the O_{III} peak at the higher binding energy ($\sim 532.2 \text{ eV}$) is related to the existence of weakly bonded oxygen species on the surface, associating with H_2O , $-\text{CO}_3$ and other chemisorbed species [47, 48]. It is noted that the O_{III} peaks (weakly bonded oxygen species) dominate the high-resolution O 1s spectra for the samples with NW parallel arrays directly printed onto the surface of Si/SiO₂ substrates. When XPS is performed on these printed NW arrays, the measured signals can be ensured collecting from the NWs, instead of getting influenced by the residual particles covered on the top surface of growth substrates; however, the Si/SiO₂ substrates employed in the NW arrayed samples are found to contribute significant O_{III} peaks here (Fig. S13 in the ESM). In this case, the XPS measurement is carried out on the NW growth substrates in order to minimize the effect of Si/SiO₂ substrates. Simultaneously, the area ratio of O_I/O_{II} has been widely demonstrated to evaluate the relative concentration of oxygen vacancies in the crystal [49]. In this work, these ratio values are assessed to be 0.88, 0.93, 1.06 and 1.63 for $\text{Zn}_4\text{In}_2\text{O}_7$, $\text{In}_{2.4}\text{Ga}_{0.3}\text{Zn}_{3.3}\text{O}_7$, $\text{In}_{1.8}\text{Ga}_{1.8}\text{Zn}_{2.4}\text{O}_7$, and $\text{In}_{0.3}\text{Ga}_{3.9}\text{Zn}_{1.8}\text{O}_7$ NWs, accordingly. In any case, these increasing ratios observed in both Fig. 5 and Fig. S13 in the ESM indicate the suppression of the number of typical oxygen related defects of IZO and IGZO materials (i.e., vacancies) by simply increasing the Ga concentration. The reason is that Ga–O bonds ($353.5 \text{ kJ}\cdot\text{mol}^{-1}$) are stronger as compared with the bonds of In–O ($320.1 \text{ kJ}\cdot\text{mol}^{-1}$) and Zn–O ($250 \text{ kJ}\cdot\text{mol}^{-1}$) [50]; therefore, the optimal Ga concentration can enhance the effectiveness of the oxygen bonding with metallic components and decrease the concentration of oxygen vacancies. At the same time, these oxygen

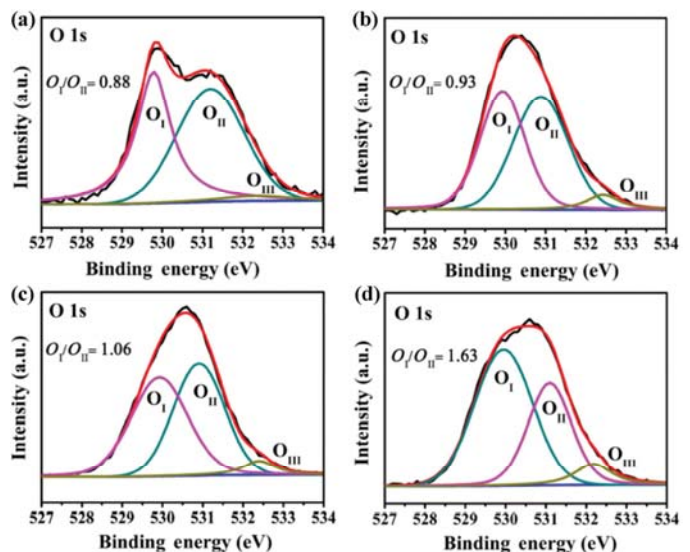


Figure 5 XPS studies of NW samples grown with the increasing mass of Ga precursor. High-resolution XPS spectra of the O 1s peak of the (a) $\text{Zn}_4\text{In}_2\text{O}_7$, (b) $\text{In}_{2.4}\text{Ga}_{0.3}\text{Zn}_{3.3}\text{O}_7$, (c) $\text{In}_{1.8}\text{Ga}_{1.8}\text{Zn}_{2.4}\text{O}_7$, and (d) $\text{In}_{0.3}\text{Ga}_{3.9}\text{Zn}_{1.8}\text{O}_7$ NWs.

vacancies generate free carriers and act as scattering centers to degrade the carrier mobility of the materials [42, 51, 52]. In this case, the reduction of oxygen vacancies by introducing Ga can yield the diminished carrier scattering for the enhanced electron mobility as well as the lessened free electron concentration for the improved on/off current ratio (i.e., gate coupling) of the NW devices. Since the too high Ga concentration would lead to the deteriorated NW crystallinity for the degraded device characteristics, combined with the superlattice-structured IGZO NW, there exists an optimal Ga concentration for the efficient modulation of carrier concentration together with the suppression of oxygen vacancy formation and minimization of grain-boundary potential barriers for the superior NW device performance.

In addition to understand their superior device performance of individual NW FETs, it is extremely important to assess their integrability for large-scale device applications, such as TFT devices. This way, the well-established NW contact printing method [53–55] is employed to fabricate the $\text{In}_{1.8}\text{Ga}_{1.8}\text{Zn}_{2.4}\text{O}_7$ NW parallel array FET. This particular NW composition is chosen here because of its best device characteristics in the above studies. All the electrical characterization are then carried out in ambient conditions in order to mimic the practical utilizations of these devices. Figure 6(a) shows the SEM image and device schematic of a typical NW parallel array FET, while Fig. 6(b) gives the corresponding transfer characteristics, exhibiting a typical n-type semiconducting behavior. When the V_{DS} is 1 V, the device can deliver a saturation current of 0.23 μA with a decent current density of $1.15 \mu\text{A}\cdot\mu\text{m}^{-1}$ and a respectable on/off current ratio of $\sim 10^5$. Also, the linear relationship of the device output characteristics in Fig. 6(c) confirms the ohmic-like contact properties between electrodes and NW parallel arrays. The corresponding field-effect electron mobility can as well be evaluated a function of gate bias voltage as in Fig. 6(d). Similar to the individual NW device, this mobility value can be calculated based on the standard square law model, where the device capacitance is determined by multiplying the capacitance of every single NW with the estimated number of NWs in the channel [56]. The peak mobility is then extracted to be $\sim 40 \text{ cm}^2\cdot\text{V}^{-1}\cdot\text{s}^{-1}$, which is comparable or even better than many state-of-the-art IGZO TFT devices shown in Fig. S14 in the ESM. This enhanced mobility can be attributed to the utilization of crystalline NW arrays as device channels over the

amorphous or polycrystalline channels of conventional TFTs. Notably, as compared with the single NW FET, the average output current of each NW gets slightly reduced in the NW parallel array device. This current reduction can be resulted by the increased parasitic capacitance owing to the misaligned or broken NW segments in the channel. In the future, optimizing the NW print density, reducing the channel length, and using the top-gated device structure with high-k dielectrics can be utilized to further improve the device performance. In any case, all these results evidently suggest the promising potency of the crystalline superlattice-structured IGZO NWs for high-performance TFT devices.

4 Conclusions

In summary, crystalline superlattice-structured IGZO NWs with different amount of Ga are successfully synthesized by an enhanced CVD method and subsequently configured into NW parallel array TFT devices. It has been shown that the Ga species play an important role in the formation of superlattice structures of IGZO, significantly affecting the electrical properties of NWs. In specific, the Ga incorporation can induce the decrease of oxygen vacancies due to the higher binding energy of Ga with oxygen, where this reduced oxygen vacancies can minimize the free electron concentration for the improved on/off current ratio as well as lessen the carrier scattering for the superior electron mobility of NW devices. However, the excessive Ga concentration can lead to the deteriorated lattice structure that can degrade the corresponding device electron mobility. More importantly, these NWs can also be integrated into parallel arrays for TFT devices, in which respectable device performance is achieved. All these results can demonstrate the promise of these crystalline superlattice-structured IGZO NWs for the practical realization of next-generation metal-oxide TFT device technologies.

Acknowledgements

This work is financially supported by the National Natural Science Foundation of China (No. 51672229), the General Research Fund (CityU 11211317) and the Theme-based Research (T42-103/16-N) of the Research Grants Council of Hong Kong SAR, China, and

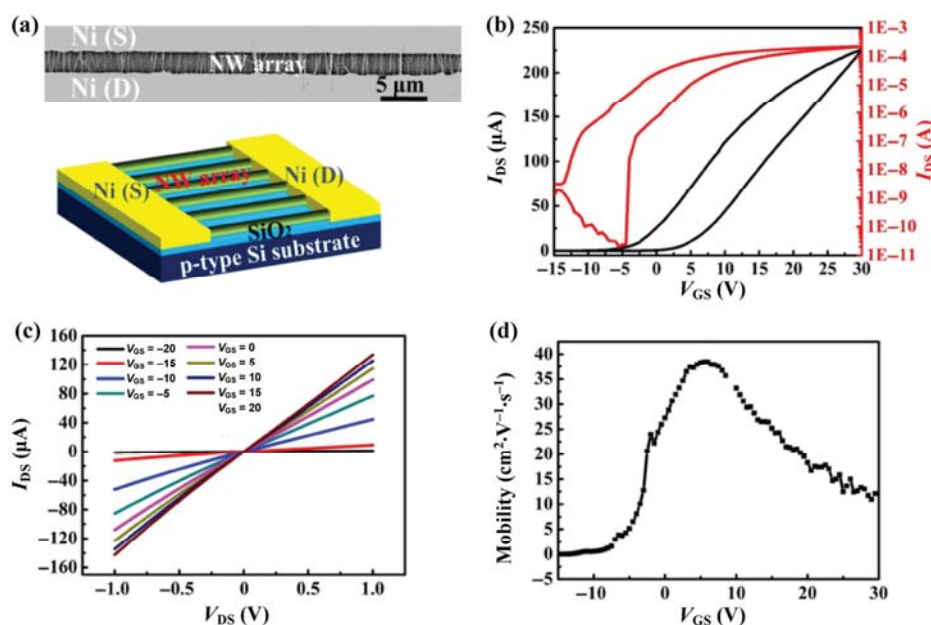


Figure 6 Electrical characterization of a typical FET based on a parallel array of $\text{In}_{1.8}\text{Ga}_{1.8}\text{Zn}_{2.4}\text{O}_7$ NWs measured in ambient conditions. (a) (Top) SEM and (bottom) device schematic of a back-gated device. (b) Transfer characteristics of the device (channel length = 2 μm ; channel width = 200 μm ; $V_{\text{DS}} = 1$ V). (c) Output characteristics of the device. (d) Mobility assessment of the device ($V_{\text{DS}} = 1$ V).

the Science Technology and Innovation Committee of Shenzhen Municipality (NO. JCYJ20170818095520778), and a grant from the Shenzhen Research Institute, City University of Hong Kong.

Electronic Supplementary Material: Supplementary material (EDS spectra, variation of the concentration of metallic components in different samples, XRD spectra, NW diameter distribution, EDS mappings, transfer and output characteristics of fabricated NW devices performed with different conditions, detailed electronic performance of these samples, XPS spectra, and comparison of the mobility among different devices) is available in the online version of this article at <https://doi.org/10.1007/s12274-019-2434-4>.

References

- Nomura, K.; Takagi, A.; Kamiya, T.; Ohta, H.; Hirano, M.; Hosono, H. Amorphous oxide semiconductors for high-performance flexible thin-film transistors. *Jpn. J. Appl. Phys.* **2006**, *45*, 4303.
- Liu, X.; Hu, H. H.; Ning, C.; Shang, G. L.; Yang, W.; Wang, K.; Lu, X. H.; Lee, W.; Wang, G.; Xue, J. S. et al. Investigation into sand mura effects of a-IGZO TFT LCDs. *Microelectron. Reliab.* **2016**, *63*, 148–151.
- Oh, H.; Cho, K.; Park, S.; Kim, S. Electrical characteristics of bendable a-IGZO thin-film transistors with split channels and top-gate structure. *Microelectron. Eng.* **2016**, *159*, 179–183.
- Wu, G. M.; Sahoo, A. K.; Lin, J. Y. Effects of e-beam deposited gate dielectric layers with atmospheric pressure plasma treatment for IGZO thin-film transistors. *Surf. Coat. Technol.* **2016**, *306*, 151–158.
- Lin, J. C.; Huang, B. R.; Yang, Y. K. IGZO nanoparticle-modified silicon nanowires as extended-gate field-effect transistor pH sensors. *Sens. Actuators, B: Chem.* **2013**, *184*, 27–32.
- Seo, D. K.; Shin, S.; Cho, H. H.; Kong, B. H.; Whang, D. M.; Cho, H. K. Drastic improvement of oxide thermoelectric performance using thermal and plasma treatments of the InGaZnO thin films grown by sputtering. *Acta Mater.* **2011**, *59*, 6743–6750.
- Andrews, S. C.; Fardy, M. A.; Moore, M. C.; Aloni, S.; Zhang, M. J.; Radmilovic, V.; Yang, P. D. Atomic-level control of the thermoelectric properties in polytypoid nanowires. *Chem. Sci.* **2011**, *2*, 706–714.
- Zhou, H. T.; Li, L.; Chen, H. Y.; Guo, Z.; Jiao, S. J.; Sun, W. J. Realization of a fast-response flexible ultraviolet photodetector employing a metal-semiconductor-metal structure InGaZnO photodiode. *RSC Adv.* **2015**, *5*, 87993–87997.
- Tsao, S. W.; Chang, T. C.; Huang, S. Y.; Chen, M. C.; Chen, S. C.; Tsai, C. T.; Kuo, Y. J.; Chen, Y. C.; Wu, W. C. Hydrogen-induced improvements in electrical characteristics of a-IGZO thin-film transistors. *Solid-State Electron.* **2010**, *54*, 1497–1499.
- Chiu, C. J.; Chang, S. P.; Chang, S. J. High-performance a-IGZO thin-film transistor using Ta₂O₅ gate dielectric. *IEEE Electron Device Lett.* **2010**, *31*, 1245–1247.
- Chen, H. T.; Cao, Y.; Zhang, J. L.; Zhou, C. W. Large-scale complementary macroelectronics using hybrid integration of carbon nanotubes and IGZO thin-film transistors. *Nat. Commun.* **2014**, *5*, 4097.
- Nomura, K.; Ohta, H.; Takagi, A.; Kamiya, T.; Hirano, M.; Hosono, H. Room-temperature fabrication of transparent flexible thin-film transistors using amorphous oxide semiconductors. *Nature* **2004**, *432*, 488–492.
- Wang, Y.; Liu, S. W.; Sun, X. W.; Zhao, J. L.; Goh, G. K. L.; Vu, Q. V.; Yu, H. Y. Highly transparent solution processed In-Ga-Zn oxide thin films and thin film transistors. *J. Sol-Gel Sci. Technol.* **2010**, *55*, 322–327.
- Nomura, K.; Ohta, H.; Ueda, K.; Kamiya, T.; Hirano, M.; Hosono, H. Thin-film transistor fabricated in single-crystalline transparent oxide semiconductor. *Science* **2003**, *300*, 1269–1272.
- Nomura, K.; Ohta, H.; Ueda, K.; Kamiya, T.; Orita, M.; Hirano, M.; Suzuki, T.; Honjiyo, C.; Ikuhara, Y.; Hosono, H. Growth mechanism for single-crystalline thin film of InGaO₃(ZnO)₅ by reactive solid-phase epitaxy. *J. Appl. Phys.* **2004**, *95*, 5532–5539.
- Ohta, H.; Nomura, K.; Orita, M.; Hirano, M.; Ueda, K.; Suzuki, T.; Ikuhara, Y.; Hosono, H. Single-crystalline films of the homologous series InGaO₃(ZnO)_m grown by reactive solid-phase epitaxy. *Adv. Funct. Mater.* **2003**, *13*, 139–144.
- Nomura, K.; Kamiya, T.; Ohta, H.; Ueda, K.; Hirano, M.; Hosono, H. Carrier transport in transparent oxide semiconductor with intrinsic structural randomness probed using single-crystalline InGaO₃(ZnO)₅ films. *Appl. Phys. Lett.* **2004**, *85*, 1993–1995.
- Chen, H. G.; Lin, Y. S. Epitaxial growth of superlattice YbGaO₃(ZnO)₅ and InGaO₃(ZnO)₅ films by the combination of sputtering and reactive solid phase epitaxy. *Thin Solid Films* **2013**, *545*, 33–37.
- Guo, Y. J.; Van Bart, B.; Locquet, J. P.; Seo, J. W. Formation of crystalline InGaO₃(ZnO)_m nanowires via the solid-phase diffusion process using a solution-based precursor. *Nanotechnology* **2015**, *26*, 495601.
- Wu, L. L.; Liu, F. W.; Chu, Z. Q.; Liang, Y.; Xu, H. Y.; Lu, H. Q.; Zhang, X. T.; Li, Q.; Hark, S. K. High-yield synthesis of In₂₋₃Ga₃O₃(ZnO)₅ nanobelts with a planar superlattice structure. *CrystEngComm* **2010**, *12*, 2047–2050.
- Jayaswal, N.; Raman, A.; Kumar, N.; Singh, S. Design and analysis of electrostatic-charge plasma based dopingless IGZO vertical nanowire FET for ammonia gas sensing. *Superlattices Microstruct.* **2019**, *125*, 256–270.
- Felizco, J. C.; Uenuma, M.; Senaha, D.; Ishikawa, Y.; Uraoka, Y. Growth of InGaZnO nanowires via a Mo/Au catalyst from amorphous thin film. *Appl. Phys. Lett.* **2017**, *111*, 033104.
- Li, D. P.; Wang, G. Z.; Yang, Q. H.; Xie, X. Synthesis and photoluminescence of InGaO₃(ZnO)_m nanowires with perfect superlattice structure. *J. Phys. Chem. C* **2009**, *113*, 21512–21515.
- Han, N.; Yang, Z. X.; Wang, F. Y.; Yip, S.; Dong, G. F.; Liang, X. G.; Hung, T.; Chen, Y. F.; Ho, J. C. Modulating the morphology and electrical properties of GaAs nanowires via catalyst stabilization by oxygen. *ACS Appl. Mater. Interfaces* **2015**, *7*, 5591–5597.
- Han, N.; Wang, F. Y.; Yip, S.; Hou, J. J.; Xiu, F.; Shi, X. L.; Hui, A. T.; Hung, T.; Ho, J. C. GaAs nanowire Schottky barrier photovoltaics utilizing Au–Ga alloy catalytic tips. *Appl. Phys. Lett.* **2012**, *101*, 013105.
- Fang, M.; Han, N.; Wang, F. Y.; Yang, Z. X.; Yip, S.; Dong, G. F.; Hou, J. J.; Chueh, Y.; Ho, J. C. III–V nanowires: Synthesis, property manipulations, and device applications. *J. Nanomater.* **2014**, *2014*, 702859.
- Hui, A. T.; Wang, F. Y.; Han, N.; Yip, S.; Xiu, F.; Hou, J. J.; Yen, Y. T.; Hung, T.; Chueh, Y. L.; Ho, J. C. High-performance indium phosphide nanowires synthesized on amorphous substrates: From formation mechanism to optical and electrical transport measurements. *J. Mater. Chem.* **2012**, *22*, 10704–10708.
- Johnson, M. C.; Aloni, S.; McCready, D. E.; Bourret-Courchesne, E. D. Controlled vapor–liquid–solid growth of indium, gallium, and tin oxide nanowires via chemical vapor transport. *Cryst. Growth Des.* **2006**, *6*, 1936–1941.
- Vomiero, A.; Ferroni, M.; Comini, E.; Faglia, G.; Sberveglieri, G. Insight into the formation mechanism of one-dimensional indium oxide wires. *Cryst. Growth Des.* **2010**, *10*, 140–145.
- Na, C. W.; Bae, S. Y.; Park, J. Short-period superlattice structure of Sn-doped In₂O₃(ZnO)₄ and In₂O₃(ZnO)₅ nanowires. *J. Phys. Chem. B* **2005**, *109*, 12785–12790.
- Wu, L. L.; Liang, Y.; Liu, F. W.; Lu, H. Q.; Xu, H. Y.; Zhang, X. T.; Hark, S. Preparation of ZnO/In₂O₃(ZnO)_m heterostructure nanobelts. *CrystEngComm* **2010**, *12*, 4152–4155.
- Jie, J. S.; Wang, G. Z.; Han, X. H.; Hou, J. G. Synthesis and characterization of ZnO:In nanowires with superlattice structure. *J. Phys. Chem. B* **2004**, *108*, 17027–17031.
- Huang, D. L.; Wu, L. L.; Zhang, X. T. Size-dependent InAlO₃(ZnO)_m nanowires with a perfect superlattice structure. *J. Phys. Chem. C* **2010**, *114*, 11783–11786.
- Cho, S. W.; Kim, J. H.; Shin, S.; Cho, H. H.; Cho, H. K. All-solution-processed InGaO₃(ZnO)_m thin films with layered structure. *J. Nanomater.* **2013**, *2013*, 909786.
- Seo, D. K.; Kong, B. H.; Cho, H. K. Composition controlled superlattice InGaO₃(ZnO)_m thin films by thickness of ZnO buffer layers and thermal treatment. *Cryst. Growth Des.* **2010**, *10*, 4638–4641.
- Kamiya, T.; Takeda, Y.; Nomura, K.; Ohta, H.; Yanagi, H.; Hirano, M.; Hosono, H. Self-adjusted, three-dimensional lattice-matched buffer layer for growing ZnO epitaxial film: Homologous series layered oxide, InGaO₃(ZnO)₅. *Cryst. Growth Des.* **2006**, *6*, 2451–2456.
- Wu, L. L.; Li, Q.; Zhang, X. T.; Zhai, T. Y.; Bando, Y.; Golberg, D. Enhanced field emission performance of Ga-doped In₂O₃(ZnO)₃ superlattice nanobelts. *J. Phys. Chem. C* **2011**, *115*, 24564–24568.
- Keem, K.; Jeong, D. Y.; Kim, S.; Lee, M. S.; Yeo, I. S.; Chung, U. I.; Moon, J. T. Fabrication and device characterization of omega-shaped-gate ZnO nanowire field-effect transistors. *Nano Lett.* **2006**, *6*, 1454–1458.
- Yang, Z. X.; Wang, F. Y.; Han, N.; Lin, H.; Cheung, H. Y.; Fang, M.; Yip, S.;

- Hung, T.; Wong, C. Y.; Ho, J. C. Crystalline GaSb nanowires synthesized on amorphous substrates: From the formation mechanism to p-channel transistor applications. *ACS Appl. Mater. Interfaces* **2013**, *5*, 10946–10952.
- [40] Yang, Z. X.; Han, N.; Fang, M.; Lin, H.; Cheung, H. Y.; Yip, S.; Wang, E. J.; Hung, T.; Wong, C. Y.; Ho, J. C. Surfactant-assisted chemical vapour deposition of high-performance small-diameter GaSb nanowires. *Nat. Commun.* **2014**, *5*, 5249.
- [41] Yang, Z. X.; Yip, S.; Li, D. P.; Han, N.; Dong, G. F.; Liang, X. G.; Shu, L.; Hung, T. F.; Mo, X. L.; Ho, J. C. Approaching the hole mobility limit of GaSb nanowires. *ACS Nano* **2015**, *9*, 9268–9275.
- [42] Li, W. Q.; Liao, L.; Xiao, X. H.; Zhao, X. Y.; Dai, Z. G.; Guo, S. S.; Wu, W.; Shi, Y.; Xu, J. X.; Ren, F. et al. Modulating the threshold voltage of oxide nanowire field-effect transistors by a Ga⁺ ion beam. *Nano Res.* **2014**, *7*, 1691–1698.
- [43] Rao, C. N. R.; Kulkarni, G. U.; Thomas, P. J.; Edwards, P. P. Size-dependent chemistry: Properties of nanocrystals. *Chem. Eur. J.* **2002**, *8*, 28–35.
- [44] Volokitin, Y.; Sinzig, J.; De Jongh, L. J.; Schmid, G.; Vargaftik, M. N.; Moisevi, I. I. Quantum-size effects in the thermodynamic properties of metallic nanoparticles. *Nature* **1996**, *384*, 621–623.
- [45] Park, G. C.; Hwang, S. M.; Choi, J. H.; Kwon, Y. H.; Cho, H. K.; Kim, S. W.; Lim, J. H.; Joo, J. Effects of In or Ga doping on the growth behavior and optical properties of ZnO nanorods fabricated by hydrothermal process. *Phys. Status Solidi A* **2013**, *210*, 1552–1556.
- [46] Li, T. C.; Han, C. F.; Kuan, T. H.; Lin, J. F. Effects of sputtering-deposition inclination angle on the IGZO film microstructures, optical properties and photoluminescence. *Opt. Mater. Express* **2016**, *6*, 343–366.
- [47] Kamiya, T.; Hosono, H. Material characteristics and applications of transparent amorphous oxide semiconductors. *NPG Asia Mater.* **2010**, *2*, 15–22.
- [48] Jeong, S.; Ha, Y. G.; Moon, J.; Facchetti, A.; Marks, T. J. Role of gallium doping in dramatically lowering amorphous-oxide processing temperatures for solution-derived indium zinc oxide thin-film transistors. *Adv. Mater.* **2010**, *22*, 1346–1350.
- [49] Zhou, Z. Y.; Lan, C. Y.; Yip, S.; Wei, R. J.; Li, D. P.; Shu, L.; Ho, J. C. Towards high-mobility In₂Ga_{2-2x}O₃ nanowire field-effect transistors. *Nano Res.* **2018**, *11*, 5935–5945.
- [50] Parthiban, S.; Kwon, J. Y. Role of dopants as a carrier suppressor and strong oxygen binder in amorphous indium-oxide-based field effect transistor. *J. Mater. Res.* **2014**, *29*, 1585–1596.
- [51] Lei, B.; Li, C.; Zhang, D.; Tang, T.; Zhou, C. Tuning electronic properties of In₂O₃ nanowires by doping control. *Appl. Phys. A* **2004**, *79*, 439–442.
- [52] Zhang, D. H.; Ma, H. L. Scattering mechanisms of charge carriers in transparent conducting oxide films. *Appl. Phys. A* **1996**, *62*, 487–492.
- [53] Hou, J. J.; Han, N.; Wang, F. Y.; Xiu, F.; Yip, S.; Hui, A. T.; Hung, T.; Ho, J. C. Synthesis and characterizations of ternary InGaAs nanowires by a two-step growth method for high-performance electronic devices. *ACS Nano* **2012**, *6*, 3624–3630.
- [54] Han, N.; Wang, F. Y.; Hui, A. T.; Hou, J. J.; Shan, G. C.; Xiu, F.; Hung, T.; Ho, J. C. Facile synthesis and growth mechanism of Ni-catalyzed GaAs nanowires on non-crystalline substrates. *Nanotechnology* **2011**, *22*, 285607.
- [55] Han, N.; Hui, A. T.; Wang, F. Y.; Hou, J. J.; Xiu, F.; Hung, T.; Ho, J. C. Crystal phase and growth orientation dependence of GaAs nanowires on Ni₃Ga₄ seeds via vapor-solid-solid mechanism. *Appl. Phys. Lett.* **2011**, *99*, 083114.
- [56] Zou, X. M.; Liu, X. Q.; Wang, C. L.; Jiang, Y.; Wang, Y.; Xiao, X. H.; Ho, J. C.; Li, J. C.; Jiang, C. Z.; Xiong, Q. H. et al. Controllable electrical properties of metal-doped In₂O₃ nanowires for high-performance enhancement-mode transistors. *ACS Nano* **2013**, *7*, 804–810.